RSC Advances

PAPER

View Article Online
View Journal | View Issue

Cite this: *RSC Adv.*, 2023, **13**, 701

Facile and scalable synthesis of un-doped, doped and co-doped graphene quantum dots: a comparative study on their impact for environmental applications†

Reena Suryawanshi, Ramsingh Kurrey, Sushama Sahu and Kallol K. Ghosh *

Received 22nd August 2022
Accepted 20th October 2022

DOI: 10.1039/d2ra05275j

rsc.li/rsc-advances

In recent years, graphene quantum dots (GQDs) received huge attention due to their unique properties and potential applicability in different area. Here, we report simple and facile method for the synthesis of GQDs and their functionalization by doping and co-doping using different heteroatom under the optimized conditions. The doping and co-doping of GQDs using boron and nitrogen have been confirmed by FTIR and TEM. The UV-visible and fluorescence techniques have been used to study the optical properties and stability of functionalized GQDs. Further, the screening for enhancement of quantum yields of all GQDs were performed with fluorescence and UV-visible spectra under the optimized conditions. The average QY was obtained as 16.0%, 83.6%, 18.2% and 29.6% for GQDs, B-GQDs, N-GQDs and B,N-GQDs, respectively. The sensor was used to determine paraoxon in water samples. The LOD was observed to be 1.0×10^{-4} M with linearity range of 0.001 to 0.1 M. The RSD was calculated for the developed B,N-GQDs based sensor and observed to be 2.99% with the regression coefficient as 0.997. All the doped, co-doped and un-doped GQDs possess remarkable properties as a fluorescent probe.

1. Introduction

Graphene quantum dots (GQDs) are new emerging members of the luminescent carbon family.[1–4] These are crystalline semiconductors prepared using graphene and single or 4–5 layered zero-dimensional graphene sheets with a diameter <20 nm of the exciton Bohr radius. GQDs exhibit remarkable physicochemical, electronic and optical (photoluminescence (PL) and electrochemiluminescence (ECL)) properties with good photostability. GQDs also exhibit multicolour emission, biocompatibility and chemical inertness derived from the quantum confinement and edge effects.[5,6] Thus, GQDs are desirable candidates for tremendous applications, including biosensing, bioimaging, optical sensing, photocatalysis, optoelectronics, *etc.*[7,8] Naik *et al.*[4] studied the effect of pH on GQDs by developing a molecular scale rapid synthetic method for GQDs using citric acid as a carbon precursor. Li *et al.*[2] developed sulphur and nitrogen co-doped GQD-assisted chemiluminescence for the sensitive detection of tryptophan and mercury in human plasma and water samples. Zhao *et al.*[60] synthesized oxygen-enriched N-GQDs *via* a green synthetic method and reported their advantages in pH-sensitive photoluminescence and mercury detection.

Recently, graphene and graphene-based materials have gained wide attention owing to various applications.[9] Doping and co-doping of GQDs with various heteroatoms, such as boron, sulphur, nitrogen, fluorine, chlorine, bromine, iodine, potassium and selenium, and co-dopants have proven to be effective approaches to modulate their intrinsic electronic, luminescence and reactive properties.[10,11] Yu *et al.*[12] studied functionalized GQDs *via* electrochemical exfoliation of carbon fibers for the detection of sulfide ions. Herein, GQDs show fascinating properties and size-dependent optical properties as an environmentally friendly system.

Huang *et al.*[13] developed a highly fluorescent nanoprobe carbon dot-desferrioxamine B (CD-DB) *via* the conjugate connection of CDs and desferrioxamine B for the detection of iron ions. The determination of the fluctuation of ascorbic acid induced by hypoxia in cells and *in vivo* system. The nanoprobe exhibited excellent sensitivity and selectivity for the detection of Fe^{3+} and AA. Since a decade, many researchers have reported the synthesis and functionalization methods of graphene based materials to enhance their application in various fields. The highly fluorescent behaviour of graphene-based materials has gained increasing attention.[14–16] GQDs were synthesized by the use of citric acid as a precursor and then characterized by fluorescence and UV-visible spectroscopic techniques. Furthermore, graphene was used as sensor for sensitive and selective

School of Studies in Chemistry, Pt. Ravishankar Shukla University, Raipur-492010, Chhattisgarh, India. E-mail: kallolkghosh@gmaill.com

† Electronic supplementary information (ESI) available. See DOI: https://doi.org/10.1039/d2ra05275j.

detection and degradation of several environmental pollutants.[17,18]

In addition, these approaches are proving graphene as an eminent sensing material for the detection of environmental and biological toxicants.[19] Doping of GQDs with B results in the generation of holes and doping with N produces electrons. In addition, co-doping of GQDs with heteroatoms is the combination of both the hole and electron production.[20,21] The doping of GQDs using B generates holes, and thus it would effectively tune the electronic nature and result in distinctive characteristics. Nitrogen atom effectively alters the properties of GQDs and enhances its application in the field of detection and degradation. According to several experimental results, nitrogen is shown to be a good candidate for chemical doping on the surface of GQDs, as their five valence electrons could easily interact with graphene atoms and form strong valence bonds.[15–17] Tam *et al.*[22] studied the one-step hydrothermal approach for the synthesis of B-GQDs using glucose and boric acid as the precursor. In this work, B-GQDs showed exceptional electrocatalytic properties than the other metal- and nonmetal-doped GQDs. Wang *et al.*[23] used 4-vinylphenylboronic acid (VPBA) and boric acid under high-temperature treatment (200 ° C) for the formation of B-GQDs. The C–H bond in the benzene ring and O–B bond in boric acid were ruptured to produce B-doped carbon-based free radicals and further formed bigger carbon-based fragments.[24–26]

Other than these, a simple, efficient, and scalable synthesis of B,N-GQDs with high quantum yield and bright fluorescence is extremely desirable. The smaller sized particle shows different characteristics than the bulk state.[27] The reduction in the size of any object tends to oppose its properties because of the high surface area to charge ratio; thus, GQDs have also been utilized for bioimaging and biosensing applications.[28] These also possess good biocompatibility, better water solubility, and low cytotoxicity; accordingly, GQDs based biosensors have been developed by doping and co-doping in order to enhance their PL properties.[29]

GQDs have been synthesized by two approaches, *i.e.*, the "top-down" and the "bottom-up". In the last few years, many researchers have synthesized GQDs using these two approaches and have been used for a wide range of applications.[30] However, most of the approaches are unsatisfactory due to the need for cost-effective equipment, rigorous solution preparation conditions, and complicated processing. Fan *et al.*[31] reported the synthesis, structure, and photoluminescence properties of GQDs for bioimaging applications. Bak *et al.*[32] developed energy related applications of GQDs, such as lithium ion batteries, solar cells, and capacitors. In comparison to the electrochemical approach, the hydrothermal method may be a better alternative due to its ease of handling and low cost of equipment. Choi *et al.*[33] used hydrothermal treatment of glucose in the presence of boric acid to create B-GQDs. The result exhibits high B contents in GQDs with uniform size in the nm scale. Wang and co-workers[34] reported the synthesis of N-GQDs with intense fluorescence through hydrothermal treatment of benzimidazoles.[35,36] The result shows that N-GQDs possess a homogeneous size at 3.8 nm scale with good crystallinity, high photostability, better water dispersibility, and a high quantum yield of about 25%.

The un-doped GQDs has relatively lower quantum yield (QY), limited sensitivity, and selectivity. To overcome this drawback, GQDs have been co-doped with different heteroatoms to enhance their fluorescence properties.[37] Such co-doping of GQDs with B and N results in a P–N junction type of semiconductor with highly stable photoluminescence and lesser toxicity than the un-doped GQDs.[38] Here, B is an electron deficient metalloid and N is an electron rich nonmetal. Doping of GQDs with N atom results in forming bonds with 4 neighbouring C atoms and the remaining 5th electron is weakly bonded to the parent atom in N-GQDs. B contains 3 electrons in its valence shell, so electron vacancies are observed, which is called as hole.[39] A P–N junction is formed by close contact of this fabricated n-type semiconductor for N-GQDs and p-type for B-GQDs. The arrangement of P–N junction for B,N-GQDs possess concentration gradient across P and N sides. Here, holes diffuse from B-GQDs to N-GQDs and electrons diffuse from N-GQDs to B-GQDs.[40] This diffusion of electrons from N-GQDs has been eliminated by recombination with B-GQDs and the same happens for the diffusion of holes on the N-GQDs. Thus, a positive charge is developed in N-GQDs and a negative charge in B-GQDs.[41] This allows their use in biosensing, bioimaging, photocatalysis, super capacitors, photovoltaic and energy storage devices, *etc.* The co-doping of GQDs provides them with a better platform to be used as a sensing material as compared to other nanomaterials.[42]

In the present investigation, the un-doped, doped, and co-doped GQDs have been successfully synthesized using B and N as heteroatoms. These graphene-based materials have been characterized by UV-visible, fluorescence, FTIR, and TEM techniques. The advantages of the doped and co-doped B,N-GQDs included a tuned band gap, improved quantum yields (QYs), ionic mobility, and electrical and optical features that are also useful in biosensing applications.[43]

2. Experimental section

2.1. Reagents and chemicals

All the chemicals and reagents used for the experiment were of analytical grade and used without further purification. Glucose (purity ≥ 99.5%), citric acid (purity ≥ 99.5%), boric acid (purity ≥ 99.5%), borax (purity ≥ 99.5%), urea (purity ≥ 99.5%), ammonia (purity ≥ 99.5%), sodium hydroxide (purity ≥ 99.5%), hydrochloric acid (purity ≥ 99.5%), and dialysis membrane (2000 dalton cut off) were purchased from Sigma Aldrich, Pvt. Ltd. Bangalore, India. Whatman filters no. 42 were purchased from Sigma Aldrich, Pvt. Ltd. Bangalore, India. Double distilled water was used throughout the experiment for the preparation of all the sample solutions.

2.2. Synthesis of graphene based quantum dots

2.2.1 Graphene quantum dots. Graphene quantum dots (GQDs) were synthesized by a facile one step bottom up method with some modification.[44] For this, 2.0 g of citric acid was

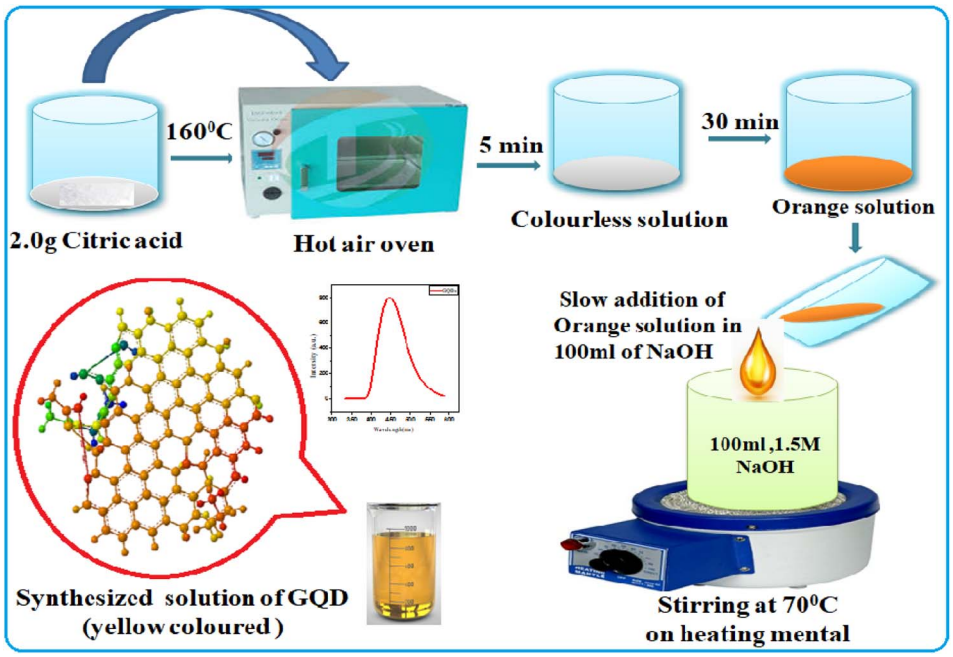

Scheme 1 Schematic representation for the synthesis of GQDs.

heated at 160 °C. After 5 min, it was liquified and then the colour of the solution changed to orange after 30 min. Afterward, 100 mL of 1.5 M NaOH was added to the above solution with vigorous stirring and the appearance of a light yellowish solution indicated the formation of GQDs.[45] Dialysis membrane is very important in GQDs synthesis to remove large particles. After cooling at RT, the obtained solution was filtered using a 0.22 μm dialysis membrane. A schematic representation of the synthesis of GQDs is shown in Scheme 1.

2.2.2 Boron doped graphene quantum dots. Boron doped graphene quantum dots (B-GQDs) were synthesized by the carbonization of glucose with boric acid following the hydrothermal method.[46] Here, 2.0 g of glucose and 8.0 mg of boric acid (0.2 wt%) were mixed with 40 mL of double distilled water under constant stirring for about 3 h at 100 rpm, and then kept in a microwave oven for heating at 70 °C. Subsequently, the solution was transferred to an autoclave and kept for 2 h at 160 °C. The solution is then purified using a dialysis membrane

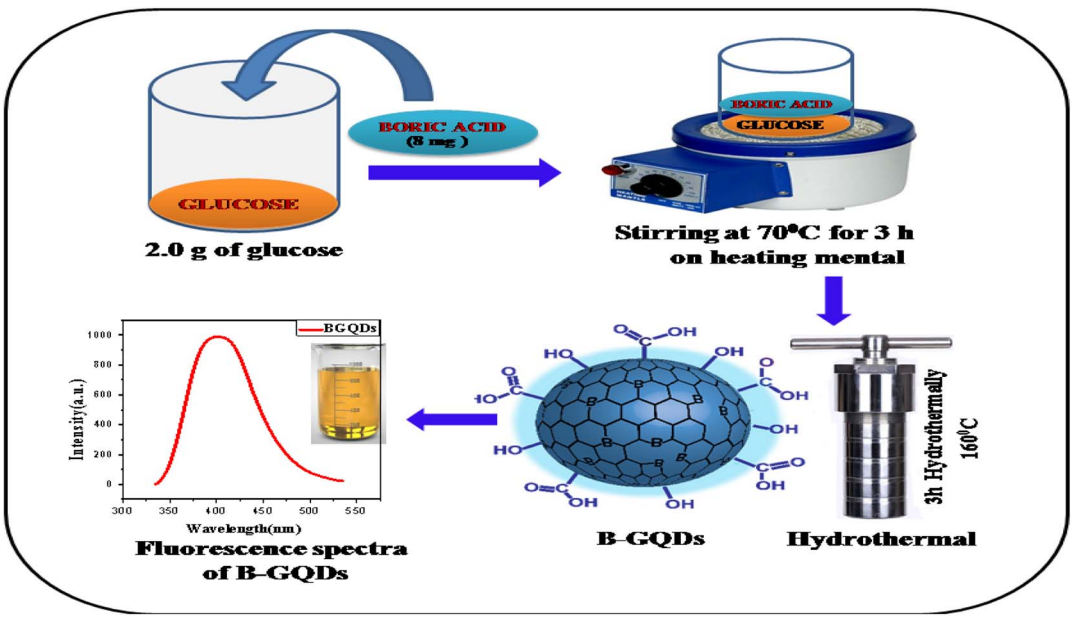

Scheme 2 Schematic representation of the synthesis of B-GQDs.

for 2 days.[47] Finally, a light yellowish solution of B-GQD was obtained, which is used as a nanosensor in further experimental procedures. The schematic representation of the synthesis of GQDs as nanosensors is displayed in Scheme 2.

2.2.3 Nitrogen doped graphene quantum dots. The schematic diagram for the preparation of N-GQDs is shown in Scheme 3. The modified N-GQDs have also been synthesized using a facile, one-step method by carbonization of glucose and urea. Here, glucose is used for C and urea as N source.[48,49] An appropriate amount of glucose was mixed in a crucible, and then the mixture was heated in a microwave oven resulting in an orange colour solution within 30 min. The light yellowish solution was obtained when the melted solution was dissolved in 100 mL of 12.5% urea. The obtained solution was kept again in a hot-air oven at 70 °C for 3 h. This solution was centrifuged several times at 2000 rpm to remove large particles. Further, the solution was dialyzed using a dialysis membrane with a molecular weight of 2000 dalton for 24 h against ultrapure water. Finally, the dispersed yellow solution of N-GQDs was used as a nanosensor in all the experiments.[50]

2.2.4 Boron nitrogen co-doped graphene quantum dots. Boron nitrogen co-doped graphene quantum dots (B,N-GQDs) as modified nanosensor were also synthesized using the bottom up approach through hydrothermal method.[51] To synthesize B,N-GQDs, 0.5 g citric acid, 0.3 g urea, and 0.1 g boric acid were heated in a crucible at 200 °C for 3 h in a microwave oven. Then, the obtained greenish yellow solution was dialysed for 24 h using a 2000 dalton dialysis membrane of 0.22 μm pore size. Finally, the obtained solution was used for further characterization and applications.[52] The schematic diagram of the synthesis of modified B,N-GQDs is shown in Scheme 4.

2.3. Instrumentation

The absorption spectra of different nanosensors, such as GQDs, B-GQDs, N-GQDs and B,N-GQDs, were recorded using UV-visible spectroscopy (Cary 60, Agilent Technologies) in the range of 200–800 nm by employing 1.0 cm quartz cell at room temperature. The fluorescence spectroscopic studies of all the samples were carried out using the Cary eclipsed fluorescence spectrophotometer (Agilent Technology) in the range of 200 to 500 nm. Fourier transform infra red (FTIR) spectra of GQDs, B-GQDs, N-GQDs, and B,N-GQDs systems were studied using a Nicolette is10 (Thermo Fisher Scientific instrument calibrated with 32 scans at 4 cm^{-1} resolution). The FTIR spectrum of all the samples was investigated in the 400 cm^{-1} to 4000 cm^{-1} range. Transmission electron microscopy (JEOL, TEM-2100F) was used to find the size and morphology of GQDs, B-GQDs, N-GQDs, and B,N-GQDs. Phase identification of GQDs was performed by X-ray diffraction (XRD) analysis. The GQDs was captured by scanning electron microscope (SEM) (JEOL JSM-6701F FE-SEM) for size determination.

2.4. Studies of quantum yield

All the fluorescent materials show quantum yield due to their better electron releasing characteristics and electronegativity. For studying the quantum yield (QYs) of these materials, a 0.01 M stock solution of quinine sulphate was used as reference material.[53] UV-visible technique was used to fix the absorbance of the quinine sulphate at 0.1, 0.25, 0.50, 0.75, and 1.0 a.u. and then characterized by fluorescence spectroscopy. For example, the calculated QY of B,N-GQDs at 1 a.u. is determined in fluorescence spectra at the excitation of 300, 310, 320,

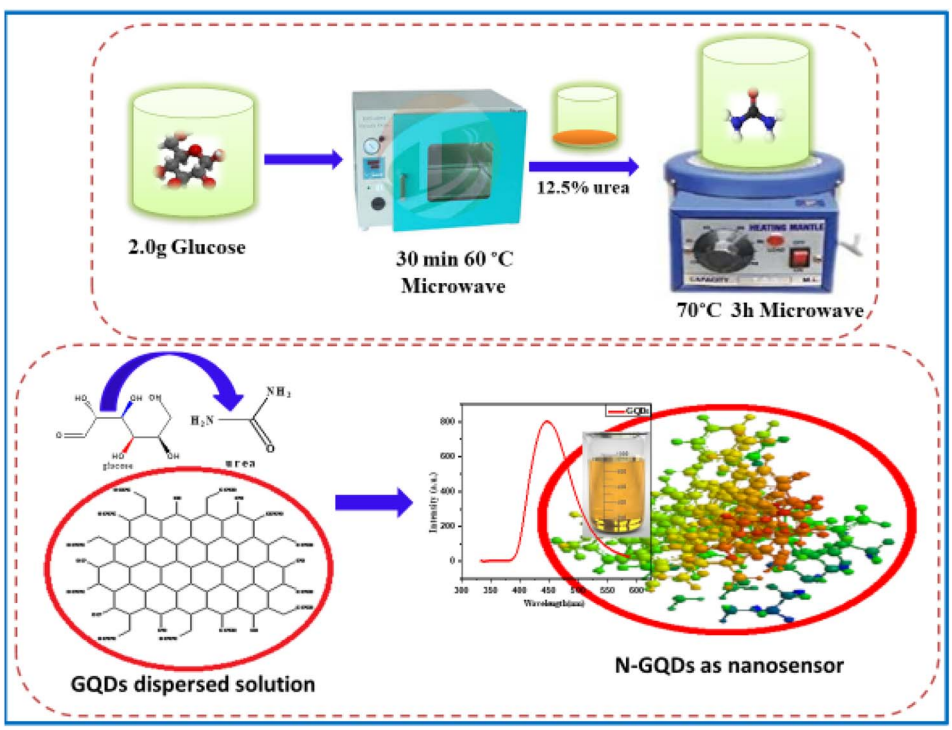

Scheme 3 Schematic representation of the synthesis of N-GQDs.

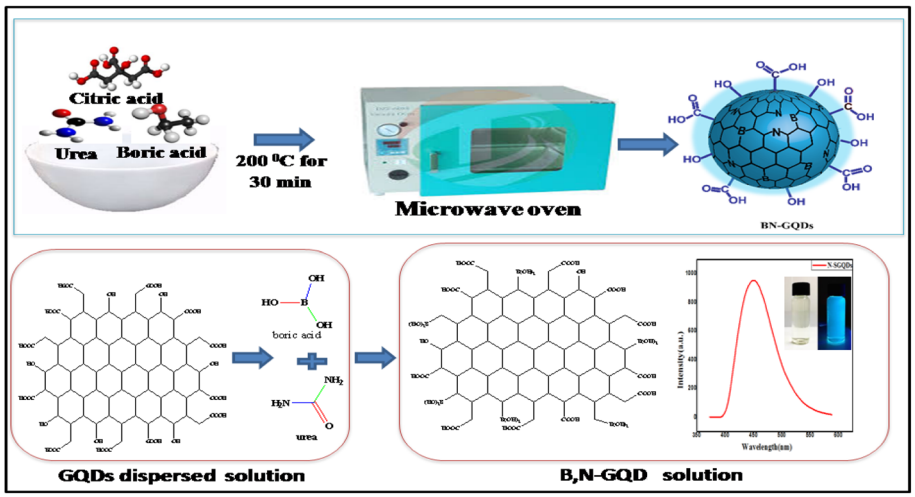

Scheme 4 Schematic representation of the synthesis of B,N-GQDs.

330, and 340 nm. Here, the fluorescence intensity of B,N-GQDs increases with absorbance at 0.2, 0.5, and 0.75 a.u. and red shifting of spectra has been observed.[54,55] The observed values have then been used for the calculation of quantum yields. The quantum yield ($\emptyset$) is a measure of the efficiency of photon emission as defined by the quantity of photons emitted divided by the number of photons absorbed and it could be calculated using eqn (1).

$$\emptyset_s = \emptyset_r \left(\frac{m_s}{m_r}\right)\left(\frac{n_s}{n_r}\right)^2 \quad (1)$$

where, $\emptyset_s$ is QY with respect to the reference-quinine in 0.1 M H_2SO_4, $\emptyset_r$ is the reference of QY, m_s and m_r are extracted from the calibration curve, while n_s and n_r represent refractive indices of the sample and reference materials, respectively.[56] In this study, various parameters, including the effect of pH, time, temperature, and concentration of GQDs have been optimized, which can affect the experimental results and enhancement of QYs.

3. Results and discussion

3.1. Optical studies

The optical properties of un-doped, doped, and co-doped GQDs are intriguing due to its tunable energy band gap. Theoretically, all the QD show similar absorption spectra with a prominent peak.[57] Here, optimization of the un-doped, doped, and co-doped GQDs has been carried out by studying the effect of temperature, concentration, time, and pH. The optical properties of the synthesized un-doped, doped, and co-doped GQDs (GQDs, B-GQDs, N-GQDs, and B,N-GQDs) have been studied using UV-visible spectroscopy in the range of 200–500 nm. Among different GQDs, a prominent spectrum has not been shown by GQDs. Further, an intense spectrum is observed for co-doped B,N-GQDs, as compared to that of B-GQDs and N-GQDs (Fig. 1(a)). The absorption band of B,N-GQDs appears at around 365 nm owing to the π–π^* transition from the aromatic sp^2 domain of GQDs into the visible range of n–π^* transition.[58] The absorption band of B-GQDs and N-GQDs appeared at 295 and 350 nm, respectively.

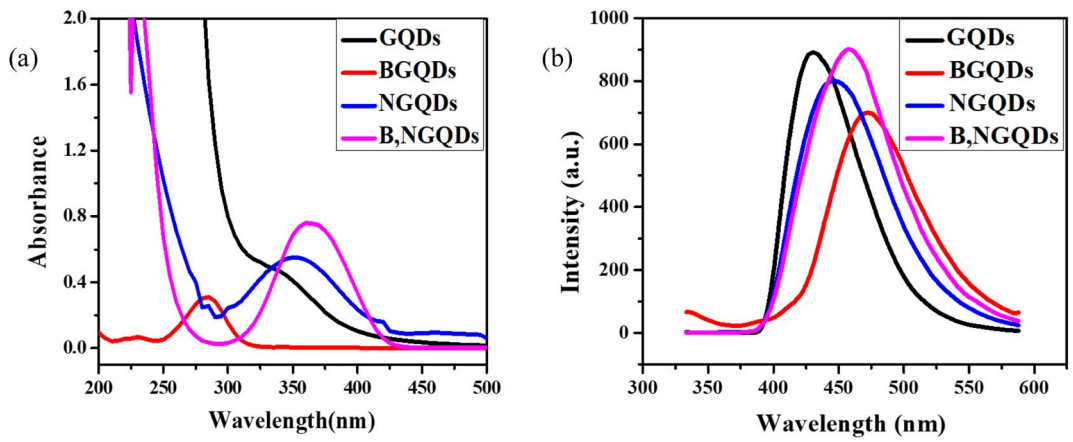

Fig. 1 (a) UV-visible and (b) fluorescence spectra of GQDs, B-GQDs, N-GQDs and B,N-GQDs.

The fluorescence study has also been performed to determine the stability and quenching phenomenon of different heteroatoms with GQDs. Herein, the colour of the dispersed GQDs is observed to be pale yellow under visible light in contrast to the greenish-blue fluorescence. In comparison to GQDs, N-GQDs and B,N-GQDs show a broad blue PL under irradiation by 365 nm. Fig. 1(b) shows the fluorescence spectra of GQDs, B-GQDs, N-GQDs, and B,N-GQDs at the excitation wavelength of 330, 310, 350, and 365 nm, respectively, by taking the slit width as 5 nm.[59] The spectrum shows a gradual red shift with an increase in the excitation for N-GQDs and B,N-GQDs, whereas a blue shift in the spectrum is observed with a decrease in the excitation wavelengths for GQDs and B-GQDs. B-GQDs shows the red shifting of spectra by 25 nm than GQDs and N-GQDs shows red shifting by 20 nm than GQDs. The shifting in the emission spectrum has been observed due to the presence of both the holes and electrons and the smaller particle size.

Further, the fluorescence spectra of GQDs, B-GQDs, N-GQDs, and B,N-GQDs at different excitation wavelengths are shown in Fig. 2(a–d). All the samples were excited at wavelengths of 330, 310, 350, and 365 nm and the fluorescence (FL) emission peaks were observed at 430, 465, 450, and 460 nm, respectively. The study confirms that the intensity of the spectra increases on increasing the excitation range. In the case of B-GQDs, a decrease in the fluorescence intensity is observed with an increase in the excitation due to the electron withdrawing characteristics of B.[60,61] While an increase in the fluorescence intensity has been shown with an increase in the excitation for N-GQDs due to the electron donating characteristics of N. Nonetheless, in the case of B,N-GQDs, when excitation increases from 300 to 340 nm, the fluorescence intensity decreases, while further increase in the intensity is observed in the range 350 to 400 nm due to the presence of electrons and holes in the lattice structure of B,N-GQDs. We also describe the excitation-wavelength-independent PL for GQDs, B-GQDs, N-GQDs, and B,N-GQDs that arises due to $\pi^* \rightarrow$ n recombination. This involves the scattering phenomenon and an electron transition and relaxation from $\sigma^* \rightarrow \pi^*$ orbital, which are essential for PL emission induced by short-wavelength excitation.[62,63] In addition, evidence suggested that the nature of PL spectrum depends on the pH, solvent, and counter ions, even in a similar size. The emission kinetics of both the GQDs and N-GQDs were multiexponentially fitted using time constant.

Further, the average fluorescence decay time of GQDs ($\tau 0$ = 513 ns), B-GQDs ($\tau 0$ = 83 ns), N-GQDs ($\tau 0$ = 71 ns), and B,N-GQDs ($\tau 0$ = 911 ns) were calculated using the weighted average process.[64] Subsequently, multiexponential dynamics arising from the surface traps of B-GQDs, N-GQDs and B,N-GQDs decrease and the redox energy level shifts to lower energies, compared to un-doped GQDs. The average decay time of co-doped GQDs increases rapidly. As a result of these findings, heteroatoms such as B and N and their mixture have been effectively doped in GQDs.

3.2. Functional group and structural elucidation

In this work, the surface of GQDs were modified with boron and nitrogen and initially characterized by simple and sensitive UV-visible and fluorescence spectroscopic techniques. According to the literature review, the presence of intermediate surface states

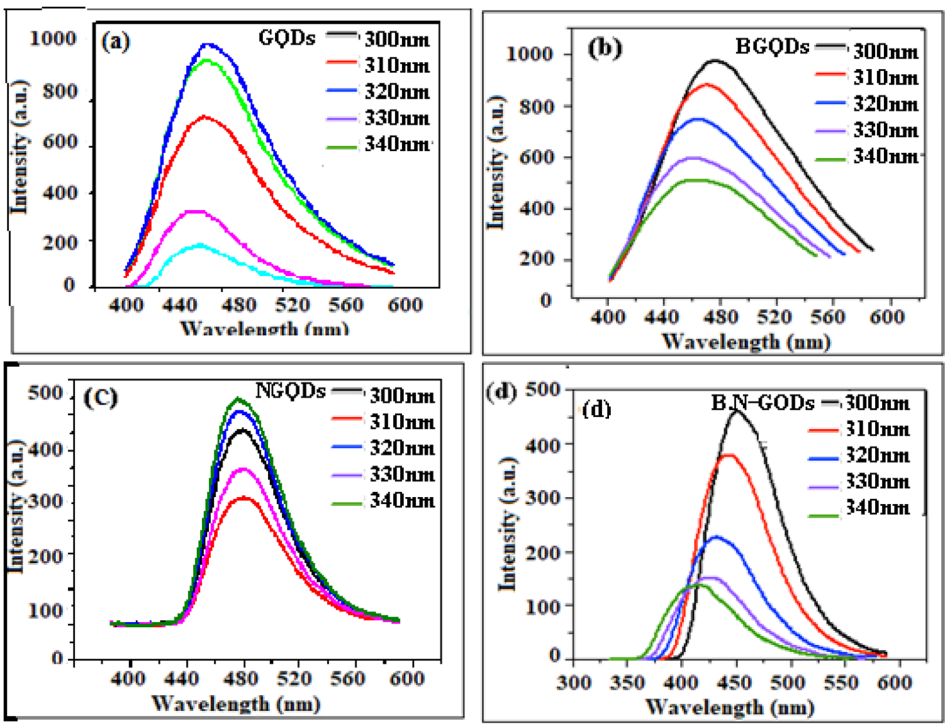

Fig. 2 Fluorescence spectra of (a) GQDs, (b) B-GQDs, (c) N-GQDs and (d) B,N-GQDs along with different excitation wavelength.

created upon functionalisations with different capping agents could be responsible for the excitation dependence, whereas excitation independent PL behaviour probably comes from the inter-band transition of doped and co-doped GQD structures.[65,66] In order to understand the intrinsic functional groups generated during the synthesis of the samples, the analysis of functional groups has been carried out for un-doped, doped, and co-doped GQDs. Fig. 3(a–h) and Table 1 show the FTIR spectrum and characteristic transmission peaks of synthesized GQDs, B-GQDs, N-GQDs, and B,N-GQDs. The FTIR absorption spectrum of GQDs is depicted in Fig. 3(b). Besides, graphene peaks at 3400.18 and 1563.80 cm^{-1} are attributed to the C–OH bond. Hence, the confirmation of graphene structure was validated by FTIR study. The characteristic FTIR absorption

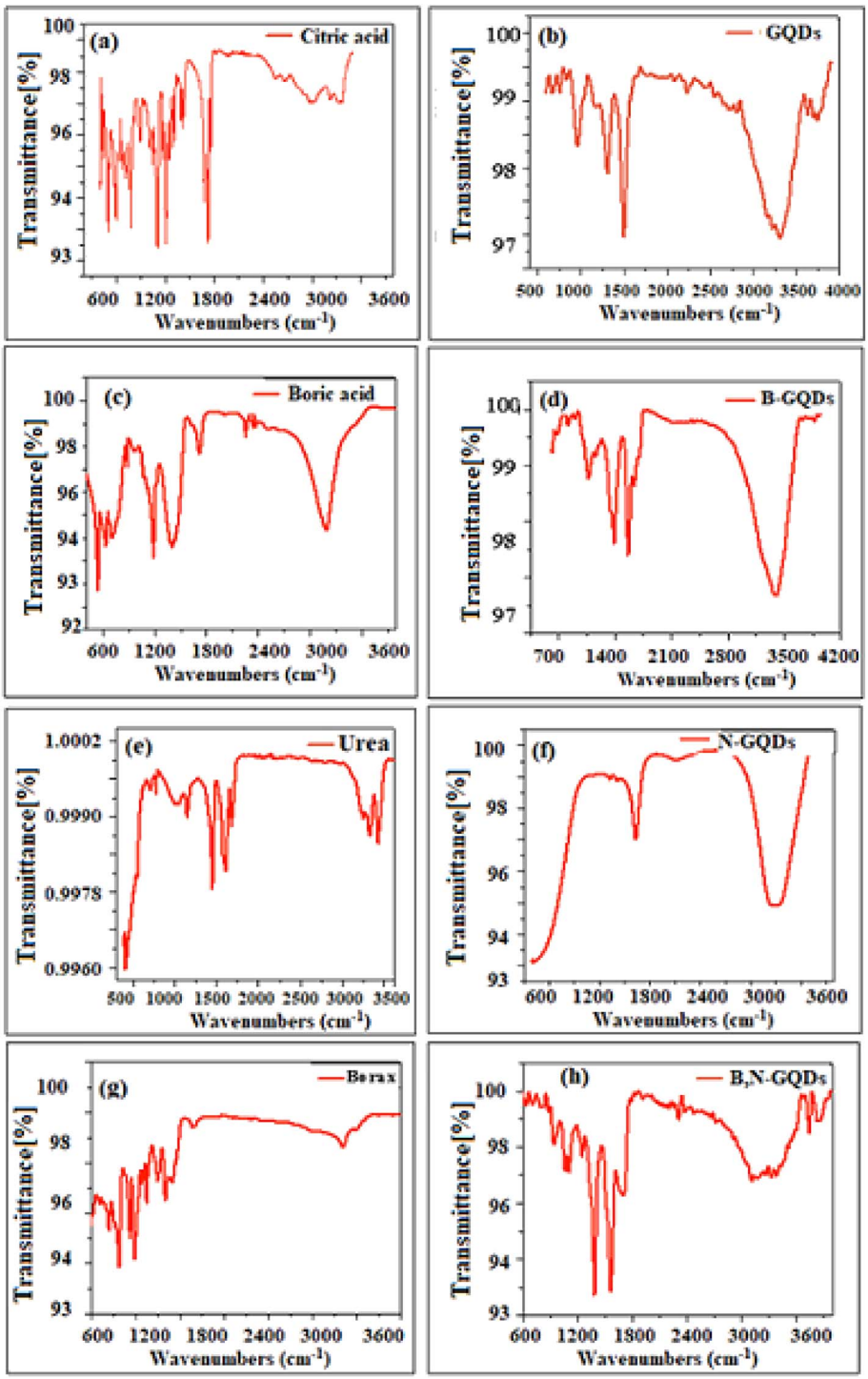

Fig. 3 FTIR spectra of (a) citric acid, (b) GQDs, (c) boric acid, (d) B-GQDs, (e) urea, (f) N-GQDs, (g) borax and (h) B,N-GQDs in the transmittance mode.

Table 1 Fourier transform infrared transmittance band and different modes of vibrations for GQDs, B-GQDs, N-GQDs and B,N-GQDs as nanomaterials

S. no.	Sample	Precursor	Group	Peak assignment	FTIR transmittance band regions (cm^{-1})	
					Present method	Reference method
1	GQDs	Citric acid	Alkyl chain	C–H asymmetrical stretching	2972	3000–2800
			Carbonyl	C=O stretching vibration	1739	1739–1700
			Hydroxyl	O–H stretching vibration	3808	3808–3500
			Aromatic hydrocarbon chain	C=C stretching vibration	1602	1602–1600
2	B-GQDs	Boric acid	Tetrahedral boron	B–O–H bending vibration	600	600–800
			Trigonal boron	B–O stretching vibration	1800	1800–900
			Hydroxyl	O–H stretching vibration	3416	3416–3500
			Carbonyl	C=O stretching vibration	1714	1714–1700
3	N-GQDs	Urea	Hydroxyl	O–H stretching vibration	3500	3500–3000
			Amine	N–H stretching vibration	3200	3200–3000
			Carboxylic	COOH bending vibration	1709	1709–1650
			Amide	CONH bending vibration	1667	1667–1600
			Carbonyl	C=O stretching vibrations	1720	1720–1700
4	B,N-GQDs	Borax	Hydroxyl	O–H stretching vibrations	3400	3400–3000
			Alcoholic-hydroxyl	H–O–H bending vibrations	1650	1650–1600
			Trigonal boron	B–O stretching vibration	1130	1130–1050
			Amine	N–H stretching vibration	3241	3241–3000
			Alkyl chain	C–H asymmetrical stretching	2946	2946–2900
			Carbonyl	C=O stretching vibration	1652	1652–1600

spectrum of citric acid used as a precursor for the synthesis of GQDs is shown in Fig. 3(a). Here, a characteristic transmission peak was observed at 3290.12 cm^{-1} (R–C(O)–OH symmetric stretching), 1721.69 cm^{-1} (C(O)–OH stretching), 1105.85 cm^{-1} (C–OH stretching vibration), and 778.78 cm^{-1} (CH_2 rocking).[67] The result is attributed to the vibration modes of citric acid molecule. The FTIR spectrum of GQDs shows a broad peak due to the –OH stretching at 3408 cm^{-1} and C=O vibration adsorption of –COOR moieties at 1739 cm^{-1}. Typical peaks at 2972 and 1602 cm^{-1} indicate the C–H asymmetric and symmetric vibrations and aromatic C=C skeletal ring vibrations from the graphitic domain, respectively (Fig. 3(b)). The frontier orbital hybridization and functional groups of GQDs reduce the energy gap between HOMO and LUMO, while the charge transfer was observed from GQDs moiety to functional groups.[68] It is also observed that all the functional groups are responsible for tailoring the electronic and optical properties of GQDs compared to other groups, which indeed has a much weaker influence on electronic structure.[69]

The FTIR spectra of boric acid used as a precursor for the formation of B-GQDs are shown in Fig. 3(c and d). It is especially difficult to assign the peaks for tetrahedral boron, as peaks from B–O–H bending, trigonal B–O stretching, and tetrahedral B–O stretching occur in the 600–1800 cm^{-1} spectral region.[70] Here, any significant shift in the spectrum is not observed due to the asymmetrical crystal structure of –OH, resulting in a horizontal axis of rotation.[71,72] However, in aqueous solution, the movement of H around the O atom of boric acid is essentially unconstrained. The FTIR transmittance peaks arising at 3416 and 1714 cm^{-1} correspond to –OH and C=O stretching vibration modes, respectively, which indicated the presence of hydroxyl and carboxyl groups on the surface of B-GQDs and endowed them with good water-solubility.[73]

The FTIR spectra of glucose and urea used for the formation of N-GQDs are shown in Fig. 3(e and f). Here, the peaks appeared at 3000–3500 cm^{-1}, which are assigned to stretching vibration of –OH and –NH groups of glucose and urea. The vibrational stretching band of C=O in the –COOH and –CONH groups on the surface of N-GQDs are ascribed to the bands at 1709 and 1667 cm^{-1}, respectively.[69] The results indicated that the surface of N-GQDs is successfully modified with urea. Kumler and Fohlen[24,74,75] interpreted the dipole moment of urea as indicating a resonance hybrid with 25–30% contribution of highly polar structures. They also pointed out that the structure of urea does not differ significantly from that of simple amides. A variety of research work assigned the C=O stretching vibrations only, which does not exist in the spectrum of *O*-alkyl derivatives of iso-urea type (I). This only indicated the $-NH_2$ group and did not address C=O.[76]

Subsequently, the FTIR spectra of borax decahydrate were collected for the qualitative determination of chemical structure. Fig. 3(g and h) shows the transmittance spectra of the pure crystals in the range of 400–4000 cm^{-1}. The bands appeared at 3400 and 1650 cm^{-1}, representing the O–H stretching and H–O–H bending vibrations, respectively.[77] The peak observed at 1432 cm^{-1} is attributed to the asymmetric stretching of the B–O bond in BO_3. Similarly, the strong transmission bands at 1130 and 1080 cm^{-1} are characteristics of asymmetric stretching of the B–O bond in BO_4.[78] Two bands appearing at 950 and 830 cm^{-1} denoted the presence of symmetric stretching of B–O in BO_3 and BO_4, respectively, which plays a key role for the binding on the surface of GQDs and resulting in the formation

of B,N-GQDs as fluorescence sensor. The appearance of all these bands confirms the formation of borax decahydrate crystals. FTIR spectroscopy was systematically applied to explore the information about the number of bonds present in the synthesized B,N-GQDs as nanomaterials.[79] The peak that appeared at 3409, 3241, 2946, and 1652 cm^{-1} are recognized as the stretching vibrations of O–H, N–H, C–H, and C=O, respectively. The strong and sharp bands that appeared at 1548 cm^{-1} are assigned to the bending vibration of N–H corresponding to an interlayer spacing of about 0.385 nm, which is larger than graphene (0.335 nm) due to the presence of multifunctional groups on the surface of B,N-GQDs. The transmittance bands of B–O stretching, B–N bending, and B–O–H bending vibrations appeared at 1380, 1215, and 1151 cm^{-1}, respectively. In comparison to pure N-GQDs, the appearance of new transmittance peaks of B–O at 1450 cm^{-1} and C–B at 1190 cm^{-1} indicated that B has been successfully doped into the GQDs network, validating the doping of B,N on graphene structure.[80] In addition, the FTIR spectral result showed the shifting of all these bands, which clearly indicated the intermolecular interaction taking place within B,N-GQDs.

3.3. Size determination of graphene based materials

TEM imaging was performed to find the crystal structure and size of all the samples (Fig. 4). Here, GQDs are spherical in shape with an average size of 2.83 ± 0.24 nm. The lattice spacing of B-GQDs is 0.16 ± 1.21 nm, corresponding to the

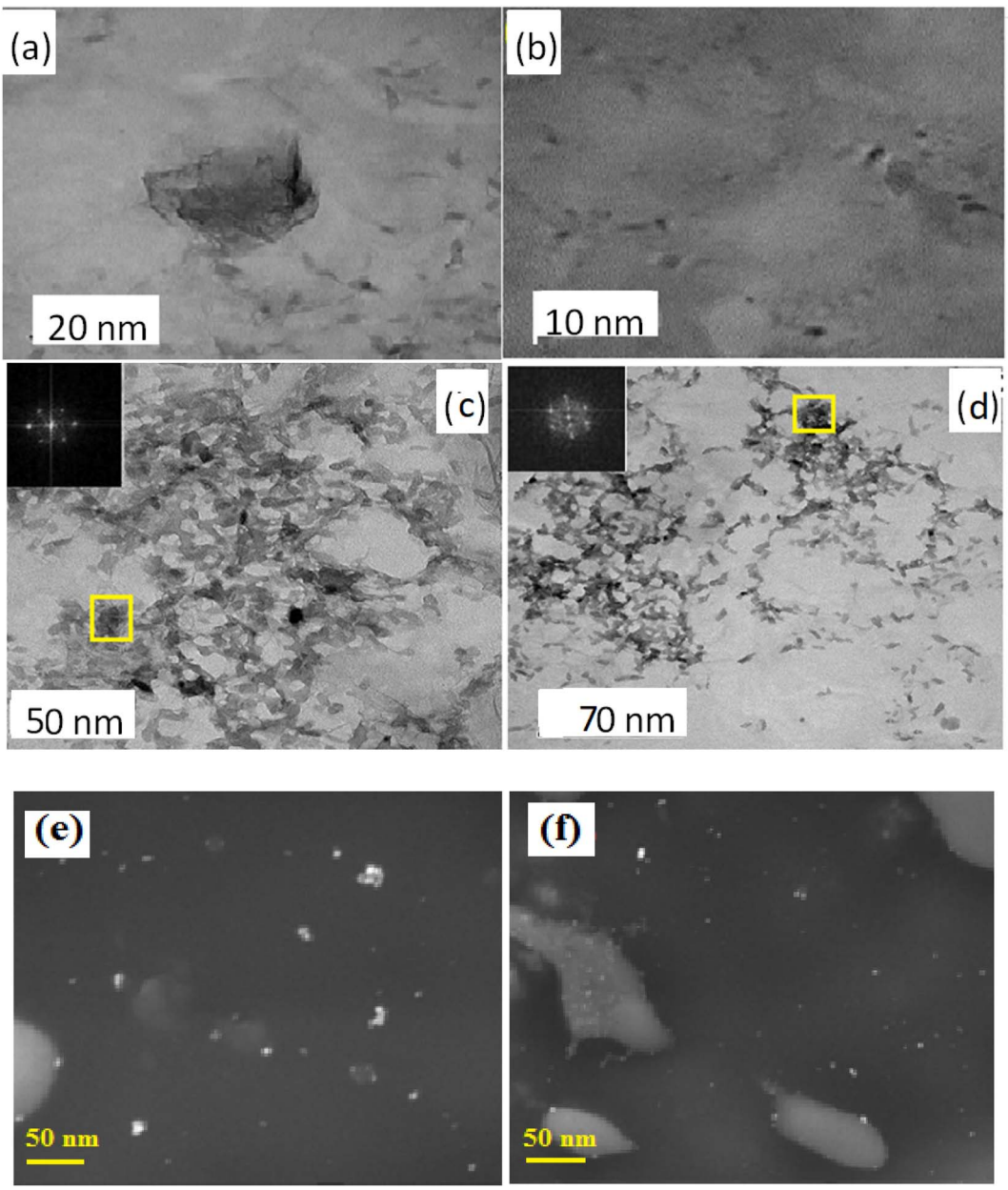

Fig. 4 TEM images of (a) GQDs, (b) B-GQDs, (c) N-GQDs and (d) B,N-GQDs. SEM images of (e) GQDS and (f) B,N-GQDs.

lattice plane of graphite, suggesting that the synthesized B-GQDs have excellent crystallinity.[81] The TEM image shows the N-GQDs exhibiting an average particle size of ~4.0 nm with a distribution of 1.6 to 2.5 nm range (Fig. 4(c)). The effect of growth time on the morphology and the size of N-GQDs was investigated from 3 to 5 min. Consequently, the size of N-GQDs has been observed at 5–10 nm. Further increase in the growth time did not affect the size and thickness of the N-GQDs. TEM image of the resultant co-doped B,N-GQDs exhibits an average particle size of ~4.0 nm with a distribution of 2.8 to 6.2 nm range.[82] The result reveals that the size of un-doped, doped, and co-doped GQDs was below the range of 2–10 nm, which is quite similar to the previously reported size of GQDs.[83] TEM imaging was performed to determine the crystal structure and size of all the samples (Fig. 4), where GQDs are spherical with an average size of 2.83 ± 0.24 nm. The TEM images have now been replaced with images of clearly visible GQD particles. This was confirmed by SEM images of the synthesized materials, which revealed no significant differences in particle size (Fig. 4(e and f)).

3.4. X-ray diffraction and zeta potential

The lattice spacing or the degree of (graphene-like) crystallinity was determined by performing additional experiments using X-

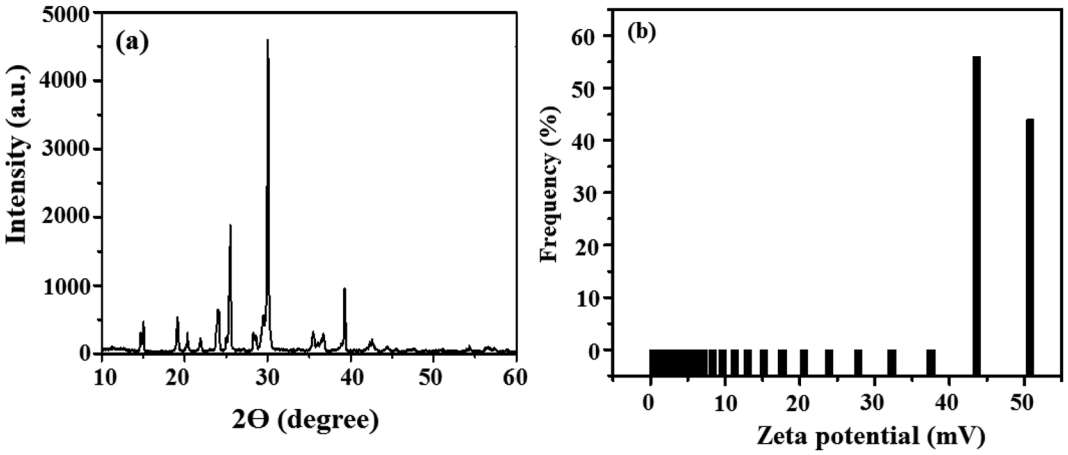

Fig. 5 (a) XRD and (b) zeta potential spectra of pure GQDs.

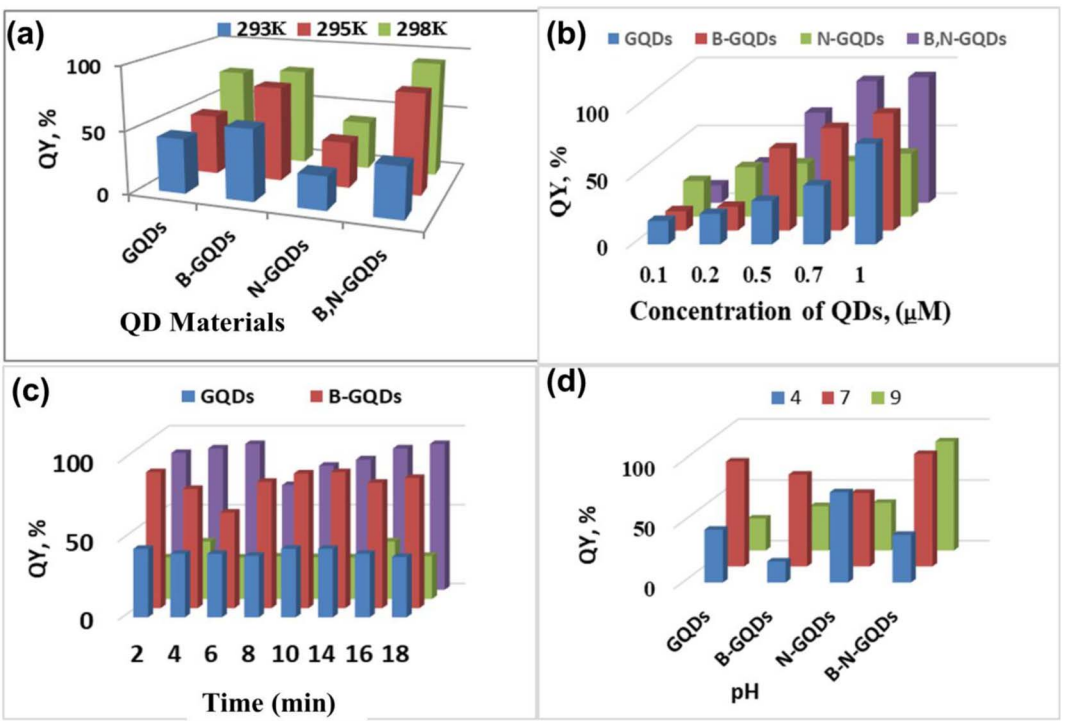

Fig. 6 3D graphical representation for the screening of QYs along with different physical parameters: (a) temperature, (b) concentration, (c) time and (d) influence of pH.

ray diffraction (XRD) technique, TEM, and SEM. The X-ray diffraction (XRD) analysis revealed the crystallinity and phase of the material. GQDs exhibited peaks at 20.09° and 30.11° for graphene oxide and 25.47° for graphite. This result is supported by the FTIR spectrum and characteristic transmission peaks of graphene-like nanostructures. The FTIR peaks of graphene at 3400.18 and 1563.80 cm^{-1} are attributed to the C–OH bond. The zeta potential value of GQD is −17.5 mV, as shown in Fig. S4.† This indicates that more electron-rich functional groups ($–NH_2$, –OH, $–CONH_2$) are present on the surface of the carbon dots. The results are shown in Fig. 5(a and b).

3.5. Screening for the enhancement of quantum yield of un-doped, doped, and co-doped GQDs

Quantum yield (QY) is one of the most important photophysical parameters when characterising luminescent materials.[84] It could be defined as the efficiency to convert absorbed light into emitted light, which can be in the form of fluorescence. The fluorophores with high QYs emit strong fluorescence even at lower concentrations. This reduces the amount of fluorophores required for an application and this subsequently cuts the cost of materials and promotes better clearance from the body for *in vivo* applications.[85] A wide range of QY values for GQDs has been observed in which the commonly reported ones are below 10%, especially those for bare or un-doped GQDs as these are obtained without surface passivation. Some studies reported that the QY values of GQDs can be altered *via* surface functionalization or doping approaches. Most of these studies showed enhancement in fluorescence intensity and QY values of 0.

In this present investigation, the screening for the enhancement of QYs of un-doped, doped, and co-doped GQDs were performed using fluorescence and UV-visible techniques under the optimized conditions.[86] QY of GQDs has been improved by varying the content of hydroxyl groups, whereas the doping of B into GQDs produces high QY (83.6%) as compared to un-doped GQDs. Similarly, QY of B-GQDs has been improved by varying the content of tetrahedral B, whereas the doping by N into GQDs produces the QY as 18.2%. Co-doping of GQDs by N and B as heteroatom increases the QY to 29.6%.

The QY of all these systems has been studied at different times, temperature, and pH to optimize the proposed sensing system. The study showed that there is no sequential alteration in the calculated values of QY (Fig. 6). This confirms that the proposed method is independent of the environmental conditions studied here. The work reported high QY for B-GQDs, but it is comparatively less stable, and thus it has been diminished. A good QY was observed for co-doped GQDs with better stability.[87] Fig. S1–S4† shows a comparison of the PL emission spectra of GQDs, B-GQDs, N-GQDs, and B,N-GQDs as a function

Table 2 QYs of different graphene based nanomaterials with respect to PL excitation and emission under optimized conditions

Concentration, mM					
QD material	Maximum PL excitation, nm	Emission, nm	QYs, %	Temperature, °C	Stability time (month)
GQDs	330	435	16.0	160	3–4
B-GQDs	270	460	83.6	160	2–3
N-GQDs	360	450	18.2	70	6–7
B,N-GQDs	360	445	29.6	200	9–12

Table 3 QY values of GQDs with desired concentrations with respect to different PL excitation, time, temperature and pH values

	Values of QY in percentage (%)													
	Time, min								Temperature, °C			pH		
QD materials	2	4	6	8	10	14	16	18	305	298	295	4	7	9
GQDs	43.5	40.33	40.31	39.1	43.53	43.5	44.33	44.36	43.5	48.33	74.31	42.1	17.33	74.31
B-GQDs	75.7	60.65	80.2	85.24	86.4	86.4	79.7	82.65	56.4	75.7	78.65	56.4	60.65	75.7
N-GQDs	26.12	26.21	26.27	27.01	36.51	26.35	27.27	36.51	26.35	36.51	39.27	26.01	36.24	38.21
B,N-GQDs	86.06	86.12	88.42	89.49	90.82	92.01	92.23	92.42	39.66	79.61	92.42	76.61	89.61	92.42

Concentration, mM					
QD materials	0.1	0.2	0.5	0.7	1.0
GQDs	17.33	22.53	32.1	43.5	74.3
B-GQDs	14.24	17.5	60.65	75.7	86.4
N-GQDs	26.35	36.51	39.27	41.01	46.54
B,N-GQDs	12.82	29.66	66.49	89.61	92.42

of excitation wavelengths 330, 310, 350, and 365 nm, respectively. The first peak is most probably triggered by singlet to singlet relaxation, whereas the second is produced by the triplet to singlet transition (as the triplet excitons tend to have longer diffusion lengths). Mueller *et al.*[88] explored the shifting in the peak position with different solvents and also the effect of solvent and size on singlet/triplet splitting. Similar kinds of PL peaks have been observed in the GQDs prepared by the thermal plasma jet. Here, excitation dependence is caused by intermediate surface states, which were formed after functionalization with different heteroatoms. The excitation independent PL is most likely driven by the internal GQDs structure and inter-band transition according to the findings of this work.[93] Fig. S5† shows the PL, QY and absorbance, which are directly correlated to the concentration term using Beer–Lambert law, $A = €cl$, where, A = absorbance, € = molar extinction coefficient, c = concentration, and l = path length. The equation also reveals an absorbance region corresponding to the average maximum QY (65%) for Gaussian behavior.[89] The results of this experiment are summarized in Tables 2 and 3.

Considering the discussion in the section above, only those photons cause a reaction, which are absorbed by the reactant

Table 4 Comparison of the QYs for un-doped, doped and co-doped GQDs with other reported methods along with different physical parameters and synthetic protocols

Quantum dots	Quantum yield, %	Excitation, nm	Emission, a.u.	Temperature, °C	Solvent	Stability, month	Reference material	Ref.
GQDs	8.98	310	335	170	H_2SO_4	2–3	Quinine sulphate	37
GQDs	18.0	310	335	200	ND	1–2	Fluorescein	38
B-GQDs	11.4	290	460	ND	ND	6–7	Quinine sulphate	39
B-GQDs	23.0	290	460	ND	DMF	ND	Quinine sulphate	40
N-GQDs	49.8	350	450	160	H_2SO_4	3–4	Quinine sulphate	41
N-GQDs	49.8	350	450	160	H_2SO_4	3–4	Quinine sulphate	42
B,N-GQDs	29.1	365	440	200	NH_3	3–4	Quinine sulphate	43
B,N-GQDs	52.8	365	440	160	ND	3–4	Quinine sulphate	44
GQDs	16.0	330	435	160	H_2SO_4	3–4	Quinine sulphate	**Present method**
N-GQDs	83.6	270	460	70	H_2SO_4	2–3		
B-GQDs	18.2	360	450	160	H_2SO_4	6–7		
B,N-GQDs	29.6	360	445	200	H_2SO_4	9–12		

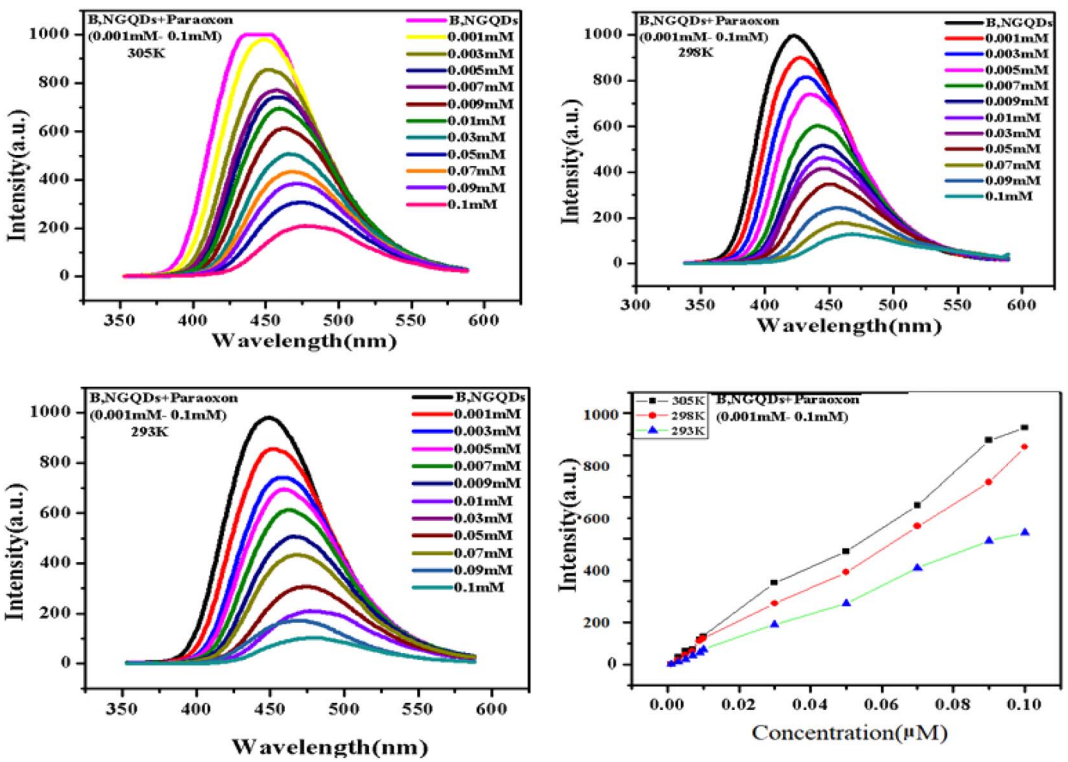

Fig. 7 Fluorescence spectra of B,N-GQDs at different temperatures and paraoxon concentrations.

starting the photo primary step. Solvent polarity, viscosity, rate of solvent relaxation, probe, conformational changes, rigidity of the local environment, and internal charge transfer could also affect the fluorescence emission spectra and QYs.[90] Therefore, H_2SO_4 was chosen on the basis of polarity, viscosity, and all the above chemical properties.

3.6. Comparison of the QYs with previously reported methods

Table 4 provides the physicochemical parameters for screening QY using UV-visible and fluorescence techniques and has been compared with the previously reported literature in terms of the precursor and synthesis methodologies. The synthesis of GQDs using a hydrothermal method provided high QYs, showing the advantages of doped and co-doped GQDs as a sensing system. The obtained results of QYs for four different kinds of graphene based materials in an aqueous solution have been compared with several reported nanomaterials, like graphene, graphene oxide, nano tubes, nanowires, quantum wire and so on.[91,92] In the present investigation, many folds enhancement in the fluorescence signal intensity and better QY has been observed as compared to those of other hydrothermal, precursor pyrolysis acid catalysed, solvothermal, and ultrasonic treatment procedures. The proposed method shows high adsorption efficiency, requires minimal time, shows good stability, is easy to handle and eco-friendly, and do not require any sophisticated instrument for the screening of QYs.[93–95] The average QYs for the proposed systems were obtained as 16.2%, 83.6%, 18.2%, and 29.6% for GQDs, B-GQDs, N-GQDs, and B,N-GQDs, respectively. The present study indicated that quinine sulphate plays a key role for the determination of QY than the other reference materials. The highly stable GQDs possess better stability and PL properties than the low yielded QDs.[96,97]

3.7. Determination of Stern–Volmer and binding constant using fluorescence spectrophotometry

The fluorescence quenching constant (K_{sv}) and binding constant (K_a) is determined to study the interaction phenomenon of B,N-GQDs with paraoxon. The study showed a decrease in the fluorescence intensity with an increase in temperature for B,N-GQDs–paraoxon system (Fig. 7). Additionally, quenching in the spectrum has been observed with increasing the concentration of paraoxon from 0.001 to 0.1 M.[98,99] The fluorescence

Table 5 Binding constant and thermodynamic parameters for the B,N-GQDs–paraoxon system

S. no.	Temperature (K)	Stern–Volmer quenching constant (K_{sv}) (10^4 L mol^{-1})	pH	Binding constant (K_a) (10^4 L mol^{-1})
1	305 K	110	7	6.5×10^{-2}
2	298 K	190	7	1.6×10^{-4}
3	293 K	60	7	1.4×10^{-4}

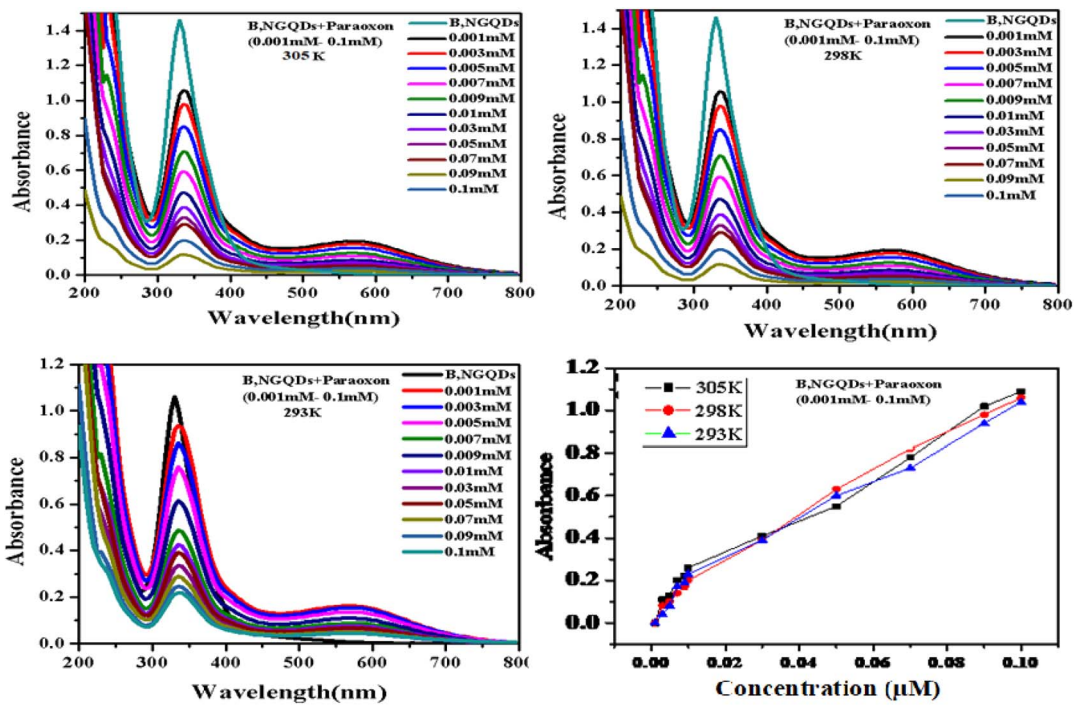

Fig. 8 UV-visible spectra of B,N-GQDs with different paraoxon concentrations and temperatures.

quenching could be calculated using the following Stern–Volmer equation.

$$\frac{F_o}{F} = 1 + K_{sv}[Q] \quad (2)$$

where K_{sv} is Stern–Volmer quenching constant, F_o is the FL intensities in the absence of a quencher (paraoxon) and F represents FL intensities in the presence of a quencher. [Q] is the concentration of analyte (paraoxon). The values of K_{sv} and K_a have been summarized in Table 5. The decrease in the value of K_{sv} with an increase in the concentration of paraoxon suggested that the interaction is static in nature as there is no shifting in spectrum observed.[100,101]

Further, the binding constant (K_a) has been analyzed by the double logarithmic equation, and observed values are summarized in Table 5.

$$\log\frac{F_o - F}{F} = \log K_a + n\log[Q] \quad (3)$$

The result demonstrated that the values of binding constant K_a increase dramatically with temperature, showing that B,N-GQDs has better binding ability towards paraoxon.

3.8. Evaluation of binding constant and thermodynamic parameters by UV-vis spectroscopy

UV-visible absorption spectrum of B,N-GQDs–paraoxon system is also demonstrated at different temperatures (Fig. 8). Here, co-doped B,N-GQDs shows a peak at 340 nm, which is related to the π–π* transition of the C=C bonds. The binding constant of B,N-GQDs–paraoxon system has been determined using the following equation.[102,103]

$$\frac{1}{A - A_o} = \frac{1}{K(A_{max} - A_o)[Q]} + \frac{1}{A_{max} - A_o} \quad (4)$$

where, A_o and A are the absorbance of B,N-GQDs in the absence and presence of paraoxon, respectively. A_{max} is the absorbance at high concentrations of paraoxon and K indicates the binding constant. Further, different thermodynamic parameters,

Table 6 Binding constant and thermodynamics parameters for B,NGQDs–paraoxon system

S. no.	Temperature (K)	Binding constant (K_a)	ΔH [kJ mol^{-1}]	ΔS [J mol^{-1} K^{-1}]	ΔG [kJ mol^{-1}]
1	305	14.86	−64	19.8	−556
2	298	14.46	−61	17.5	−479
3	293	14.09	−57	13.14	−337

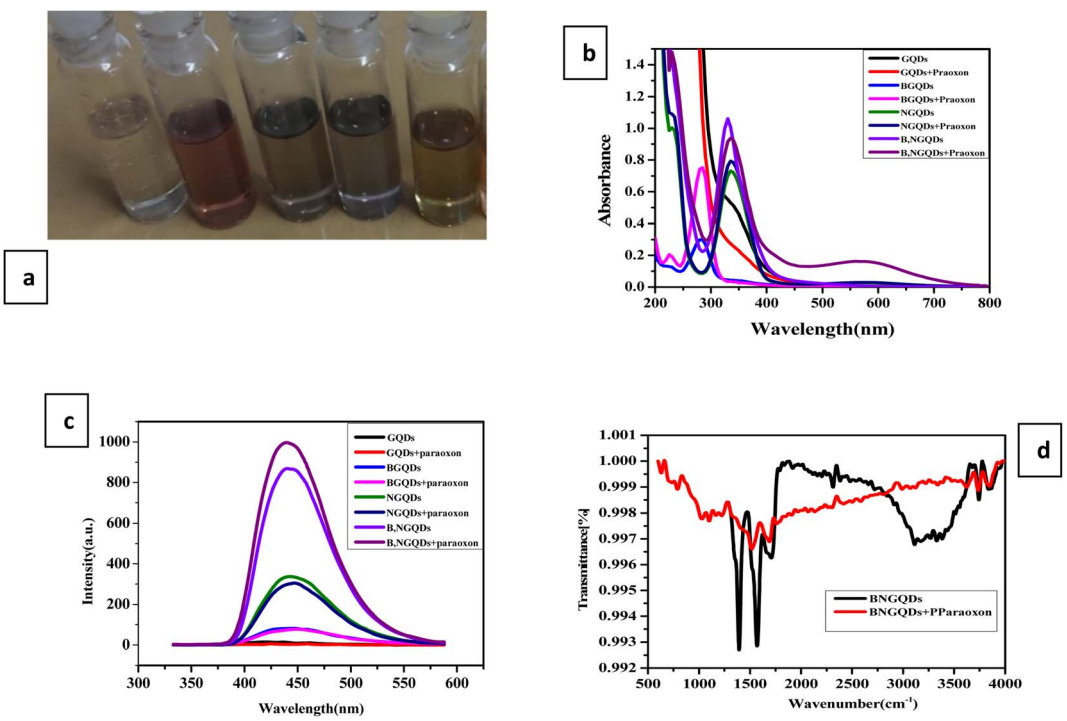

Fig. 9 Glass vial images of standard solution of paraoxon with and without the presence of GQDs, B-GQDs, N-GQDs and B,N-GQDs (a), UV-visible (b), fluorescence (c) and FTIR spectra (d) for the screening of different GQDs and paraoxon concentrations.

including Gibb's free energy (ΔG), entropy (ΔS), and enthalpy (ΔH), have been calculated (Table 6) for the B,N-GQDs–paraoxon system at the temperature of 293, 298 and 305 K, using the equations:

$$\ln K_a = -\frac{\Delta H}{RT} + \frac{\Delta S}{R} \quad (5)$$

$$\Delta G = \Delta H - T\Delta S \quad (6)$$

4. Application in real samples

Detection of paraoxon in real samples (water) is crucial because of its high toxicity and wide existence in the environment.[102] The fluorescence emission of B,N-GQDs shows more quenching behaviour with paraoxon than the other un-doped, doped, and co-doped GQDs. It has been observed that the paraoxon shows noticeable quenching with B,N-GQDs, which proved that B,N-GQDs is a rapid and better probe for detection of different environmental toxicants.[104] Fig. 9 confirms that B,N-GQDs shows an additional peak at 585 nm after complexation with paraoxon. This has also been confirmed by taking the fluorescence spectra of un-doped, doped, and co-doped GQDs, where only B,N-GQDs gives efficient quenching in the spectrum with paraoxon. Thus, the proposed system is observed to be highly stable and selective for the detection of different analytes. Further, analytical evaluation has also been carried out for B,N-GQDs–paraoxon system by studying the linearity range, limit of detection (LOD), incubation time, and correlation coefficient in a specific pH range.[105,106] FTIR spectra of B,N-GQDs with and without the addition of paraoxon were systematically applied to explore the information about the number of bonds present in the synthesized nanomaterials. The detailed information about the number of functional groups present in B,N-GQDs are discussed in the above paragraph. The sensor is used to determine paraoxon in water samples. The LOD is observed to be 1.0×10^{-4} M in the range of 0.001 to 0.1 M. The relative standard deviation is calculated for the developed B,N-GQDs based sensor and is observed to be 2.99% with the regression coefficient of 0.997.[107]

5. Conclusions

Herein, we evaluate a route for the detection of environmental pollutants such as organophosphate pesticides. The incorporation of heteroatoms such as B and N into graphene materials is a current research concern. Boron and nitrogen co-doped graphene quantum dots (B,N-GQDs) are synthesized by a one-step bottom-up hydrothermal method. The detection of paraoxon is based on the colour change of B,N-GQDs. B,N-GQDs exhibits single/bilayer graphene structure, high crystallinity, large surface to volume ratio, biocompatibility, *etc.*, by which it has drawn increasing attention in the detection and removal of pesticides. In this work, doped GQDs show fascinating properties and size dependent optical properties as an environmentally friendly system. The doped GQDs are imperative for researchers to design novel hybrid materials for better applications. Despite extensive investigations, studies based on the detection of environmental pollutants using heteroatom doped GQDs. The detection of organophosphate pesticide paraoxon and a comparative study of the screening of QYs of un-doped, doped and co-doped GQDs to find out the better stability of the material is also performed. The optical properties of the synthesized graphene-based materials were studied using UV-visible and fluorescence spectroscopy. FTIR technique has been used to confirm the surface functionalities of GQDs by B and N atoms. The effect of pH has been studied with GQDs, B-GQDs N-GQDs, and B,N-GQDs and pH significantly affects B-GQDs, N-GQDs and B,N-GQDs than the un-doped GQDs. Through the characterizations, it is confirmed that the doping and co-doping elements successfully attached onto the surface of GQDs and showed good QYs. The doped and co-doped GQDs also indicated a highly graphene-stacked structure with good crystallinity. All un-doped, doped, and co-doped GQDs possess remarkable properties, which make them suitable as fluorescent probes. A white luminescence was seen in the as-synthesized doped and co-doped GQDs in a gel-like form, with two emission zones of 400–550 nm and 550–700 nm, which is believed to have interesting applications in light-harvesting devices and optoelectronics.

Conflicts of interest

There are no conflicts of interest declared by the authors.

Acknowledgements

Authors are thankful to the Director, National Center for Natural Resources (NCNR), Raipur [Grant No: IR/SO/LU/0008/2011(SERB)] and Director, IIT MUMBAI for providing FTIR and TEM facilities, respectively. The authors wish to thank the Head, School of Studies in Chemistry, Pt. Ravishankar Shukla University, Raipur, and C. G. for providing lab facilities.

References

1 L. Feng, Z. Qin, Y. Huang, K. Peng, F. Wang, Y. Yan and Y. Chen, Boron-sulfur- and phosphorus-doped graphene for environmental applications, *Sci. Total Environ.*, 2020, **698**(1), 134239.
2 R. Li, Q. Li, A. R. B. Méndez, T. Hayashi, B. Wang, A. Berkheimer, Q. Hao, A. L. Elías, R. C. Silva, H. R. Gutiérrez, Y. A. Kim, H. Mura Matsu, J. Zhu, M. Endo, H. Terrones, J. C. Charlie, M. Pan and M. Terrones, Nitrogen Nitrogen-doped graphene: beyond single substitution and enhanced molecular sensing, *Sci. Rep.*, 2012, **2**, 586.
3 P. Yang, J. Su, R. Guo, F. Yao and C. Yuan, B,N-Co-doped graphene quantum dots as fluoresecence sensor for detection of Hg2+ and F-, *Anal. Methods*, 2019, **11**, 1879–1883.

4 J. P. Naik, P. Sutradhar and M. Saha, Molecular scale rapid synthesis of graphen quantum dots (GQDs), *J. Nanostruct. Chem.*, 2017, **7**, 85–89.
5 L. Zhang, Y. Liang, Li. Ru-ping and J. D. Qui, Boron-Doped graphene quantum dots for selective glucose sensing based on the abnormal aggregation induced photoluminescence enhancement, *Anal. Chem.*, 2014, **86**, 4423–4430.
6 J. Luo, J. Wang, S. Liu, W. Wu, T. Jia, Z. Yang, S. Mu and Y. Huang, Graphene quantum dots encapsulated tremella-like $NiCo_2O_4$ for advance asymmetric super capacitors, *Carbon*, 2019, **146**, 1–8.
7 A. Suryawanshi, M. Biswal, D. Mhamane, R. Gokhale, S. Patil, D. Guin and S. Ogale, Large scale synthesis of graphene quantum dots (GQDs) from waste biomass and their use as an efficient and selective photoluminescence, *Nanoscale*, 2014, **6**, 11664.
8 S. Dey, A. Govindaraj, K. Biswas and C. N. R. Rao, Luminescence properties of boron and nitrogen doped graphene quantum dots prepared from arc-discharge-generated doped graphene samples, *Chem. Phys. Lett.*, 2014, **59**, 203–208.
9 N. Pourreza and K. Ghanemi, Determination of mercury in water and fish samples by cold vapor atomic absorption spectrometry after solid phase extraction on agar modified with 2-mercaptobenzimidazole, *J. Hazard. Mater.*, 2009, **161**, 982–987.
10 M. L. Mueller, Y. Xin, D. Bogdan and L. Li, Slow hot-carrier relaxation in colloidal graphene quantum dots, *Nano Lett.*, 2011, **11**, 56–60.
11 M. Wang, S. Guo, Y. Li, L. Cai, J. Zou, G. Xu, W. Zhou, F. Zheng and G. Guo, Direct white-light-emitting metal–organic framework with tunable yellow-to-white photoluminescence by variation of excitation light, *J. Am. Chem. Soc.*, 2009, **131**, 13572.
12 J. Yu, W. Ji, M. Arabi, L. Fu, B. Li and L. Chen, *ACS Appl. Nano Mater.*, 2021, **4**(7), 6852–6860.
13 Y. Huang, N. He, Q. Kang, D. Shen, X. Wang, Y. Wang and L. Chen, *Analyst*, 2019, **144**, 6609–6616.
14 Z. Y. Hong, S. L. Liu and D. W. Pang, *Analyst*, 2020, **145**, 3131–3135.
15 X. W. Wang, S. Yu, J. Wang, J. Yu, M. Arabi, L. Fu, B. Li, J. Li and L. Chen, *Talanta*, 2020, **211**, 120727.
16 N. Yu, H. Peng, H. Xiong, X. Wu, X. Wang, Y. Li and L. Chen, *Microchim. Acta*, 2015, **182**, 2139–2146.
17 W. Xue, J. Zhong, H. Wu, J. Zhang and Y. Chi, *Analyst*, 2021, **146**, 7545–7553.
18 Z. Liu, F. Li, Y. Luo, M. Li, G. Hu, X. Pu, T. Tang, J. Wen, X. Li and W. Li, *Molecules*, 2021, **26**(13), 3922.
19 P. Lin, J. W. Chen, L. W. Chang, J. P. Wu, L. Redding, H. Chang and Y. C. Kuo, Computational and ultrastructural toxicology of a nanoparticle, quantum dot in mice 705, in mice, *Environ. Sci. Technol.*, 2008, **42**, 6264–6270.
20 D. I. Son, K. Won, B. W. Dong, H. P. Seo, W. S. Yi, Y. Angadi, L. Chang-Lyoul and W. K. Choi, graphene quantum dots for white-light-emitting diods, *Nat. Nanotechnol.*, 2012, **7**, 465–471.
21 T. A. Tabish, M. Z. I. Pranjol, I. Karadag, D. Horsell and S. Zhang, Influence of fluorescent graphene quantum dots on trypsin activity, *Int. J. Nanomed.*, 2018, **13**, 1525–1538.
22 T. V. Tam, S. G. Kang, K. F. Babu, O. Eun-Suok, S. G. Lee, W. M. Mook and G. Choi, Synthesis of B-doped graphene quantum dots as a metal-free electrocatalyst for the oxygen reduction reaction, *J. Mater. Chem. A*, 2017, **5**, 10537–10543.
23 S. Wang, L. Zhang, Z. Xia, A. Roy, D. W. Chang, J. B. Baek and L. Dai, graphene as efficient metal-free electro catalyst for the oxygen reduction reaction, *Angew. Chem., Int. Ed.*, 2012, **51**, 4209–4212.
24 W. D. Kumler and G. M. Fohlen, the dipole moment and structure of urea and thiourea, *J. Am. Chem. Soc.*, 1992, **64**, 1944–1948.
25 N. T. N. Anh, A. D. Chowdhury and R. A. Doong, Highly sensitive and selective detection of mercury ions using N, S-codoped graphene quantum dots and its paper strip based sensing application in wastewater, *Sens. Actuators, B*, 2017, **252**, 1169–1178.
26 D. Marczewska, M. B. Adam, W. Marczewski, S. Malgorzata and B. Tarasiuk, Adsorption of selected herbicides from aqueous solutions on activated carbon, *Chemosphere*, 2019, **214**, 349–360.
27 R. Maria-Hormigos, B. Jurado-Sanchez and A. Escarna, Graphene quantum dot based micromotors: a size matter, *Chem. Commun.*, 2019, **55**, 6795.
28 T. Schiros, D. Nordlund, L. Pálová, D. Prezzi, L. Zhao, K. S. Kim, U. Wurstbauer, C. Gutiérrez, D. Delongchamp, C. Jaye, D. Fischer, H. Ogasawara, L. G. M. Petteron, D. R. Reichman, P. Kim, M. S. Hybertsen and A. N. Pasupathy, Connecting dopant bond type with electronic structure in n-doped graphene, *Nano Lett.*, 2012, **12**, 4025.
29 J. Peng, W. Gao, B. K. Gupta, Z. Liu, R. Romero-Aburto, L. Ge, L. Song, L. B. Alemany, X. Zhan, G. Gao, S. A. Vithayathil, B. A. Kaipparettu, A. A. Marti, T. Hayashi, J. J. Zhu and P. M. Ajayan, Graphene quantum dots derived from carbon fibres, *Nano Lett.*, 2012, **12**, 844–849.
30 N. Kaur and B. Kaur, Spectral studies on anthracene based dual sensor for Hg2 + and Al3 + ions with two distinct output modes of detection, *Spectrochim. Acta, Part A*, 2017, **181**, 60–64.
31 Z. Fan, Y. Li, X. Li, W. Li, W. Zhou, Z. Wang, P. G. Ding, X. Xie, Z. Kang and M. Jiang, Large-scale fabrication of heavy doped carbon quantum dots with tunable-photoluminescence and sensitive fluorescence detection, *J. Mater. Chem. A*, 2014, **2**, 8660.
32 J. Bak, M. J. Park, S. J. Kim, D. H. Wang, S. Cho, P. Bae, J. H. Park and B. H. Hong, Balancing light absorptive and carrier conductivity of graphene quantum dots for high-efficiency bulk heterojunction solar cells, *ACS Nano*, 2013, **7**, 7207.
33 H. H. Choi, H. Yang, D. J. Kang and B. J. Kim, Enhancing mechanical properties of highly efficient polymer solar

cells using size-tuned polymer nanoparticles, *ACS Appl. Mater. Interfaces*, 2015, **7**, 2668–2676.
34 T. Wang, A. Wang, R. Wang, Z. Liu, Y. Sun, G. Shan, Y. Chen and Y. Liu, *Sci. Rep.*, 2019, 1–9.
35 C. Boonta, S. Talodthaisong, C. Sattayaporn, A. Chaicham, S. Chaicham, L. Sahasithiwat and K. S. Kulchat, The synthesis of nitrogen and sulfur co-doped graphene quantum dots for fluorescence detection of cobalt(II) ions in water, *Mater. Chem. Front.*, 2020, **4**, 507–516.
36 P. R. Kharange, S. Umapathy and G. Singh, Multiple electrical phase transitions in Al substituted barium hexaferrite, *J. Appl. Phycol.*, 2017, **122**, 145107.
37 M. Ghaedi, F. Ahmadi, A. Shokrollahi and P. Hazard, Simultaneous preconcentration and determination of copper, nickel, cobalt and lead ions content by flame atomic absorption spectrometry, *J. Mater.*, 2007, **142**, 272–278.
38 M. L. Yola and N. Atar, A novel detection approach for serotonin by graphene quantum dots/two-dimensional (2D) hexagonal boron nitride nanosheets with molecularly imprinted polymer, *Appl. Surf. Sci.*, 2018, **458**, 648–655.
39 J. H. Zhang, T. Sun, A. Niu, Y. M. Tang, S. Deng and W. Luo, Perturbation effect of reduced graphene oxide quantum dots (rGOQDs) on aryl hydrocarbon receptor (AhR) pathway in zebrafish, *Biomaterials*, 2017, **133**, 49–59.
40 R. Leu, Q. Li, A. R. B. Méndez, T. Hayashi, B. Wang, A. Berkdemir, Q. Hao, A. L. Elías, R. C. Silva, H. R. Gutiérrez, Y. A. Kim, H. Muramatsu, J. Zhu, M. Endo, H. Terrones, J. C. Charlier, M. Pan and M. Terrones, Nitrogen-doped graphene: beyond single substitution and enhanced molecular sensing, *Sci. Rep.*, 2012, **2**, 586.
41 Y. Yang, Z. C. Liu, B. Gu, B. Gao, Z. Wang, Q. Guo and G. Wang, Preparation of concentration dependent nitrogen sulfur co-doped graphene quantum dots by UV irradiation and reversible optical switch of hydroxypropyl methyl cellulose, *J. Photochem. Photobiol., A*, 2021, **15**, 112977.
42 J. He, Z. Li, R. Zhao, Y. Lu, L. Shi, J. Liu, X. Dong and F. Xi, Aqueous synthesis of amphiphilic graphene quantum dots and their application as surfactants for preparing of fluorescent polymer microspheres, *Colloids Surf., A*, 2019, **563**, 77–83.
43 B. K. Jena and C. R. Raj, Gold nanoelectrode ensembles for the simultaneous electrochemical detection of ultratrace arsenic, mercury, and copper, *Anal. Chem.*, 2008, **80**, 4836–4844.
44 W. Guo, S. Hu, X. Wang, J. Zhang, L. Jin, Z. Zhu and H. Zhang, Application of ion molecule reaction to eliminate WO interference on mercury determination in soil and sediment samples by ICP-MS, *J. Anal. At. Spectrom.*, 2011, **26**, 1198–1203.
45 M. L. Yola and N. Atar, Highly sensitive fluorescence sensor for mercury(II) based on boron- and nitrogen-co-doped graphene quantum dots, *J. Electrochem. Soc.*, 2019, **166**, 1879–1883.
46 Y. J. Dai, Y. F. Jia, N. Chen, W. P. Bian, Q. K. Li and B. M. Yang, Zebrafish as a model system to study toxicology, *Environ. Toxicol. Chem.*, 2014, **33**, 11–17.
47 D. Iannazzo, A. Pistone, M. Salamo, S. Galvagno, R. Rmeo, S. V. Giofre, C. Branca and G. Visalli, Graphene quantum dots for cancer targeted drug delivery, *Int. J. Pharm.*, 2017, **518**, 185–192.
48 Y. Qing, Y. Jiang, H. Lin, L. Wang, A. Liu, Y. Cao, R. Sheng, Y. Guo, C. Fan, S. Zhang, D. Jia and Z. Boosting, Construction of hierarchical porous carbon nanosheets from template-assisted assembly of coal-based graphene quantum dots for high performance super capacitor electrodes, *Mater. Today*, 2013, **6**, 1–3.
49 Y. Dong, C. Chen, X. Zheng, L. Gao, Z. Cui, H. Yang, C. Guo, Y. Chi and C. Li, One-step and high yield simultaneous preparation of single- and multi-layer graphene quantum dots from CX-72 carbon black, *J. Mater. Chem.*, 2012, **22**, 8764–8766.
50 S. P. Nichols, A. Koh, W. L. Storm, J. H. Shin and M. H. Schoenfisch, Biocompatible materials for continuous glucose monitoring devices, *Chem. Rev.*, 2013, **113**, 2528–2549.
51 S. Gu, C. T. Hsieh, Y. Y. Tsai, Y. Ashraf, S. Gandomi, K. D. Yeom and R. S. Kihm, Juang, Sulfur and nitrogen co-doped graphene quantum dots as a fluorescent quenching probe for highly sensitive detection toward mercury ions, *ACS Appl. Nano Mater.*, 2019, **2**, 790–798.
52 K. N. Kudin, B. Ozbas, H. C. Schniepp, R. K. Prud'homme, I. A. Aksay and R. Car, Raman spectra of graphite oxide and functionalized graphene sheets, *Nano Lett.*, 2008, **8**, 36–41.
53 L. A. Ponomarenko, F. Schedin, M. I. Katsnelson, R. Yang, E. W. Hill, K. S. Novoselov and A. K. Geim, Chaotic dirac billiard in graphene quantum dots, *Science*, 2008, **320**, 356–358.
54 R. V. Goreham, K. L. Schroeder, A. Holmes, S. J. Bradley and T. Nann, Demonstration of the lack of cytotoxicity of unmodified and folic acid modified graphene oxide quantum dots, and their application to fluorescence lifetime imaging of HaCaT cells, *Microchim. Acta*, 2018, **185**, 128.
55 L. Tang, R. Ji, X. Cao, J. Lin, H. Jiang, X. Li, K. Teng, S. C. M. Luk, S. Zeng, J. Hao and S. P. Lau, Optical and electrochemical applications of silicon–carbon dots/silicon dioxide nanocomposites, *ACS Nano*, 2012, **6**, 5102–5110.
56 P. Kumar, C. Dhand, N. Dwivedi, S. Singh, R. Khan, S. Verma, A. Singh, M. K. G. S. Kumar, R. Kumar and A. K. Srivastava, Graphene quantum dots: A contemporary perspective on scope, opportunities, and sustainability, *Renew. Sustain. Energy Rev.*, 2022, **143**, 111993.
57 H. Tetsuka, R. Asahi, A. Nagoya, K. Okamoto, I. Tajima, R. Ohta and A. Okamoto, Modulated photoluminescence of graphene quantum dot in the vicinity of individual silver nano-octahedron, *Adv. Mater.*, 2012, **24**, 5333–5338.
58 J. Peng, W. Gao, B. K. Gupta, Z. Liu, R. R. Aburto, L. Ge, L. Song, L. B. Alemany, X. Zhan, G. Gao, S. A. Vithayathil, B. A. Kaipparettu, A. A. Marti, T. Hayashi, J. J. Zhu and

P. M. Ajayan, Graphene Quantum Dots Derived from Carbon Fibers, *Nano Lett.*, 2012, **12**, 844–849.

59 A. Safavi and E. Farjami, Construction of a carbon nanocomposite electrode based on amino acids functionalized gold nanoparticles for trace electrochemical detection of mercury, *Anal. Chim. Acta*, 2011, **688**, 43–48.

60 Y. Zhao, Q. Wu and D. Wang, A micro RNAs–mRNAs network involved in the control of graphene oxide toxicity in Caenorhabditis, *RSC Adv.*, 2015, **5**, 92394–92405.

61 Q. Feng, W. Xiao, Y. Liu, Y. Zheng, Y. Lin, J. Li, Q. Ye and Z. Huang, Novel synthesis of slightly fluorinated graphene quantum dots with luminescent and paramagnetic properties through thermal cutting of fluorinated graphene materials, *Materials*, 2018, **11**, 91.

62 K. Erickson, R. Erni, Z. Lee, N. Alem, W. Gannett and A. Zettl, Determination of the local chemical structure of graphene oxide and reduced graphene oxide, *Adv. Mater.*, 2010, **22**, 4467.

63 N. Suzuki, Y. Wang, P. Elwati, Z. B. Qu, K. Kim, S. Jiang, E. Baumeister, J. Lee, B. Yeom, J. H. Bahng, J. Lee, A. Violi and N. A. Kotov, Chiral graphene quantum dots, *ACS Nano*, 2016, **10**, 1744–1755.

64 G. P. C. Mello, E. F. C. Simoes, D. M. A. Crista, J. M. M. Leitao, L. P. D. Silva and J. C. G. Esteves da Silva, Glucose sensing by fluorescent nanomaterials, *Crit. Rev. Anal. Chem.*, 2019, **49**, 542–552.

65 X. T. Zheng, A. Ananthanarayanan and K. Q. Luo, Highly efficient nuclear delivery of anti-cancer drugs using a bio-functionalized reduced graphene oxide, *Small*, 2016, **16**, 1192–1201.

66 C. Gutierrez, L. Brown, C. J. Kim, J. Park, A. Pasupathy and N. Klein, Tailoring electrical conductivity of two dimensional nanomaterial's using plasma for edge electronics: A mini review, *Nat. Phys.*, 2016, 1–7.

67 M. Dutta, S. Sarkar, T. Ghosh and D. Bask, ZnO/Graphene quantum dot solid-state solar cell, *J. Phys. Chem. C*, 2012, **116**, 20127–20131.

68 X. T. Zheng, A. Ananthanarayanan, K. Q. Luo and P. Chen, Glowing graphene quantum dots and carbon dots: properties, syntheses, and biological applications, *Small*, 2015, **11**, 1620–1636.

69 B. Mandal, S. Sarkar and P. Sarkar, Theoretical studies on understanding the feasibility of porphyrin-sensitized graphene quantum dot solar cell, *J. Phys. Chem. C*, 2015, **119**, 3400–3407.

70 L. Tang, R. Ji, X. Cao, J. Lin, H. Jiang, X. Li, K. S. Teng, C. M. Luk, S. Zeng, J. Hao and S. P. Lau, Deep ultraviolet photoluminescence of water-soluble self-passivated graphene quantum dots, *ACS Nano*, 2012, **6**, 5102–5110.

71 E. Campbell, M. T. Hasan, R. Gonzalez-Rodriguez, R. Giridhar, V. Anton and C. E. Naumov, Graphene quantum dot formulation for cancer imaging and redox-based drug delivery, *Nanomedicine*, 2021, **37**, 102408.

72 R. V. Goreham, K. L. Schroeder, A. Holmes, S. J. Bradley and T. Nann, Demonstration of the lack of cytotoxicity of unmodified and folic acid modified graphene oxide quantum dots, and their application to fluorescence lifetime imaging of HaCaT cells, *Microchim. Acta*, 2018, **185**, 128.

73 R. Purbia and S. Paria, A simple turn on fluorescent sensor for the selective detection of thiamine using coconut water derived luminescent carbon dots, *Biosens. Bioelectron.*, 2016, **79**, 467–475.

74 F. Liu, M. Jang, H. Ha, J. Kim, Y. Cho and T. S. Seo, Facile synthetic method for pristine graphene quantum dots and graphene oxide quantum dots: origin of blue and green luminescence, *Adv. Mater.*, 2013, **25**, 3657.

75 Li. Yang, Y. Zhao, Y. Shi, G. Deng, L. Hou and L. Qu, An electrochemical avenue to green-luminescent graphene quantum dots as potential electron-acceptors for photovoltaics, *Adv. Mater.*, 2011, **23**, 776–780.

76 M. Fayazi, M. A. Taher, D. Afzali and A. Mostafavi, Fe3O4 and MnO2 assembled on halloysite nanotubes: A highly efficient solid-phase extractant for electrochemical detection of mercury (II) ions, *Sens. Actuators, B*, 2016, **228**, 1–9.

77 D. Jiang, Y. Chen, N. Li, W. Li, Z. Wang and J. Zhu, Graphene quantum dot based materials for sensing, bio-imaging and energy storage applications: a review, *PLoS One*, 2016, **10**, 23861–23898.

78 R. Ye, Z. Peng, A. Metzger, J. Lin, J. A. Mann, K. Huang, C. Xiang, X. Fan, E. L. G. Samuel, L. B. Alemany, A. A. Marti and J. M. Tour, Bandgap engineering of coal-derived graphene quantum dots, *ACS Appl. Mater. Interfaces*, 2015, **7**, 7041–7048.

79 Z. Yu, Z. Chen, M. Li and L. Wu, Photoluminescence responses of graphene quantum dots toward organic bases and an acid, *J. Mater. Chem.*, 2012, **22**, 3314.

80 X. Wu, F. Tian, W. Wang, J. Chen, M. Wu and J. Zhuo, Fabrication of highly fluorescent graphenequantum dots using l-glutamic acid for in vitro/in vivo imaging and sensing, *J. Mater. Chem. C*, 2013, **1**, 4676.

81 Q. Xu, Q. Zhou, Z. Hua, Q. Xue, C. Zhang, X. Wang, D. Pan and M. Xiao, Single-particle spectroscopic measurements of fluorescent graphene quantum dots, *ACS Nano*, 2014, **7**, 10654–10661.

82 Y. Liu, X. Tang, M. Deng, Y. Cao, Y. Li, H. Zheng and L. Gao, Nitrogen doped graphene quantum dots as a fluorescent probe for mercury (II) ions, *Microchim. Acta*, 2019, **186**, 140.

83 Y. Yan, J. Gong, J. Chen, Z. Zhen, W. Huang, K. P. Liu and P. Chen, Ultra-broadband, high speed, and high-quantum-efficiency photodetectors based on black phosphorus, *Adv. Mater.*, 2019, **22**, 1808283.

84 M. K. Nazeeruddin, D. Censo, R. Humphry-Baker and M. Grätzel, Highly Selective and Reversible Optical, Colorimetric, and electrochemical detection of mercury (ii) by amphiphilic ruthenium complexes anchored onto mesoporous oxide films, *Adv. Funct. Mater.*, 2006, **16**, 189–194.

85 M. V. Prabhagar, M. O. Kumar, C. Takahashi, S. Kundu, T. N. Narayan and D. K. Pattanayak, Boosting photocatalytic activity using reduced graphene oxide

(RGO)/semiconductor nanocomposites: issues and future scope, *New J. Chem.*, 2019, **510**, 587–593.

86 M. Buzaglo, M. Shtein and O. Regev, Thermally conductive graphene-polymer composites: size, percolation, and synergy effects, *Carbon*, 2018, **130**, 369–376.

87 S. Zhu, J. Zhang, S. Tang, C. Qiao, L. Wang and H. Wang, Surface chemistry routes to modulate the photoluminescence of graphene quantum dots, *Adv. Funct. Mater.*, 2012, **22**, 4732–4740.

88 M. L. Mueller, X. Yan, B. Dragnea and L. Li, Slow hot-carrier relaxation in colloidal graphene quantum dots, *Nano Lett.*, 2011, **11**, 56–64.

89 S. Zhu, J. Zhang, C. Qiao, S. Tang, Y. Li, W. Yuan, B. Li, L. Tian, F. Liu, R. Hu, H. Gao, H. Wei, H. Zhang and H. Sun, Deciphering a nanocarbon-based artificial peroxidase: chemical identification of the catalytically active and substrate-binding sites on graphene quantum dots, j. Yang, *Angew. Chem., Int. Ed.*, 2015, **54**, 7176.

90 X. Jiang, D. Qui, G. Mo, J. Feng, C. Yu and W. Mo, Novel enzymatic graphene oxide based biosensor for the detection of glutathione in biological body fluids, *Materials*, 2019, **164**, 514–519.

91 G. Rajendar, U. Goswami and P. K. Giri, Solvent dependent synthesis of edge-controlled graphene quantum dots with high photoluminescence quantum yield and their application in confocal imaging of cancer cells, *J. Colloid Interface Sci.*, 2017, **541**, 387–398.

92 C. Qu, D. Zhang, R. Yang, J. Hu and L. Qu, Nitrogen and sulfur co-doped graphene quantum dots for the highly sensitive and selective detection of mercury ion in living cells, *Spectrochim. Acta, Part A*, 2019, **206**, 588–596.

93 J. Sun, S. Yang, Z. Wang, H. Shen, T. Xu, L. Sun, H. Li, W. Chen, X. Jiang, G. Ding, X. Xie and M. Jiang, Doping: versatile graphene quantum dots with tunable nitrogen doping, *Part. Part. Syst. Charact.*, 2014, **45**, 92620–92628.

94 D. Jiang, Y. Chen, N. W. Li, Z. Wang, J. Zhu, H. Zhang, B. Liu and S. Xu, High-Resolution Analyses of Human Leukocyte Antigens Allele and Haplotype Frequencies Based on 169,995 Volunteers from the China Bone Marrow Donor Registry, *PLoS One*, 2015, **11**(9), e1005171.

95 J. Xue, X. Xu, Y. Zhu and D. Yang, Graphene/polyaniline nanorod arrays: synthesis and excellent electromagnetic absorption properties, *J. Mater. Chem. C*, 2012, **42**, 1–3.

96 K. Ghosh, M. Kumar, T. Maruyama and Y. Ando, Tailoring the field emission property of nitrogen-doped carbon nanotubes by controlling the graphitic/pyridinic substitution, *Carbon*, 2010, **48**(1), 191–200.

97 A. Ferrari, J. Meyer, V. Scardaci, C. Casiraghi, M. Lazzeri, F. Mauri, S. Piscanec, D. Jiang, K. Novoselov, S. Roth and A. Geim, *Phys. Rev. Lett.*, 2006, **97**, 187401.

98 L. Li, G. Wu, G. Yang, J. Peng, J. Zhao and J. J. Zhu, *Nanoscale*, 2013, **5**, 4015–4039.

99 Y. Dong, H. Pang, H. B. Yang, C. Guo, J. Shao, Y. Chi, C. M. Li and T. Yu, *Angew. Chem., Int. Ed.*, 2013, **52**, 7800–7804.

100 S. Kadian, G. Manik, S. M. Ashish and R. P. Chouhan, *Nanotechnology*, 2019, **30**(43), 435704.

101 S. Xue, P. Wang and K. Chen, *Spectrochim. Acta, Part A*, 2010, **20**, 10716–10723.

102 B. T. Hoan, P. V. Huan, H. N. Van, D. H. Nguyen, P. D. Tam, K. T. Nguyen and Y. H. Pham, *Luminescence*, 2017, **55**, 51–57.

103 Y. Dong, J. Shao, C. Chen, H. Li, R. Wang, Y. Chi, X. Lin and G. Chen, *Carbon*, 2012, **50**, 4738–4743.

104 X. Yan, X. Cui, B. Li and L. S. Li, *Nano Lett.*, 2010, **10**, 1869–1873.

105 J. Zhu, M. Xu, M. Gao, Z. Zhang, Y. Xu and T. Xia, *ACS Nano*, 2017, **11**, 2637–2651.

106 Z. L. Wu, M. X. Gao, T. T. Wang, X. Y. Wan, L. L. Zheng and C. Z. Huang, *Nanoscale*, 2014, **6**, 3868–3874.

107 Y. Shen, M. Rong, X. Qu, B. Zhao, J. Zha, Z. Liu, Y. Bao, Y. He, S. Li, X. Wang, M. Chen, K. Chen, Y. Zheng and L. Niu, *Talanta*, 2022, **241**, 123224.